# Retroreflector Studies

by
David A. Arnold
94 Pierce Road, Watertown, MA 02472, U.S.A.
Phone: 617-924-3811, email: david-arnold@earthlink.net
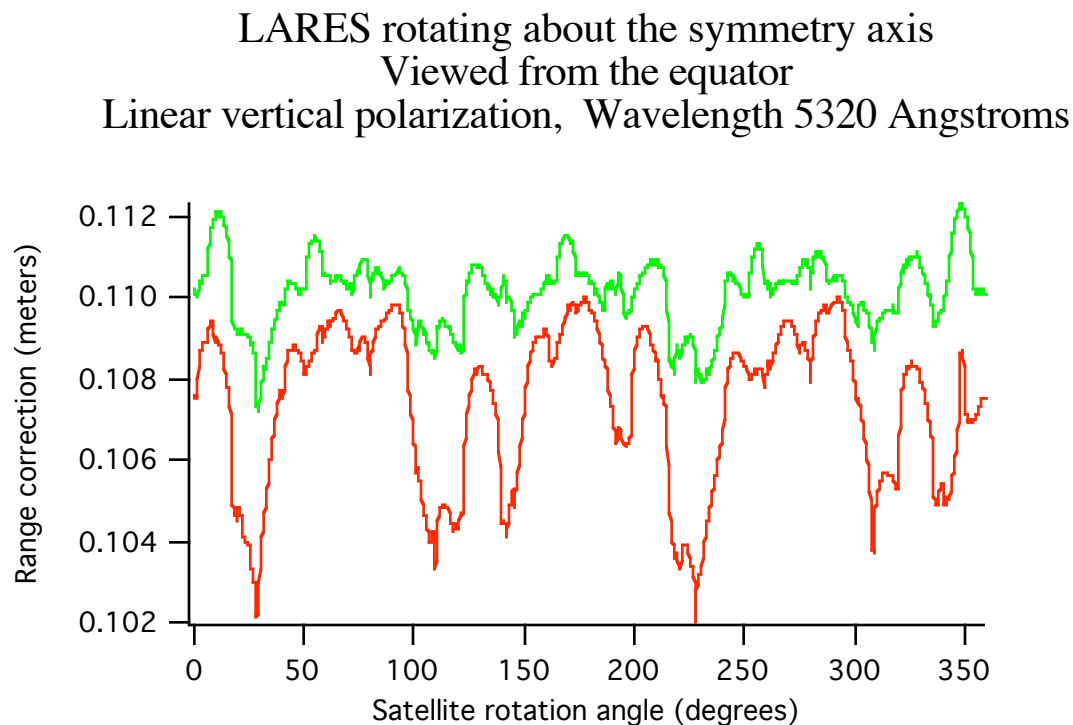
## Contents:

## 1. Introduction

There are a number of different studies of retroreflector arrays currently being done to assist in the design of future retroreflector arrays and obtain a better understanding of the properties of current retroreflector arrays. This paper gives a summary of these studies.

## 2. LARES preliminary transfer function

This section gives excerpts from a presentation at LNF in Frascati, Italy in April, 2006.

A preliminary transfer function has been computed for the current configuration of the proposed LARES satellite. The transfer function is computed from the positions and orientations of the cube corners kindly provided by Tommaso Napolitano of LFN/INFN. The proposed design uses the same type of cube corner as LAGEOS but mounted in a different sphere intended to provide better modeling of thermal thrust which is important in the scientific use of the satellite.

The figures below show how the range correction varies as the satellites rotates. This is a measure of the range accuracy. The last figure shows the corresponding variation for LAGEOS.

LARES rotating about the symmetry axis
Viewed from the equator
Linear vertical polarization,  Wavelength 5320 Angstroms



Red = centroid detection  Green = half-max detection
Receiver is on the vertical axis of the diffraction pattern
$X = 0$  microradians   $Y = 35$ microradians
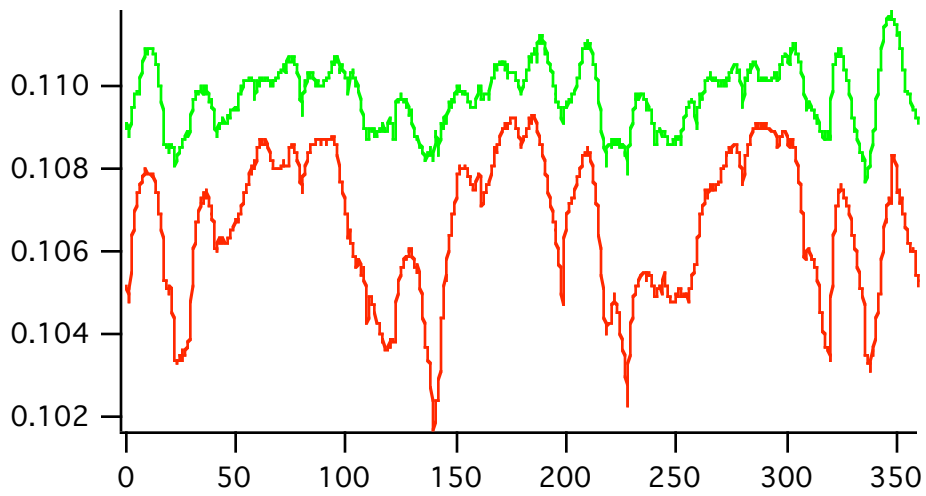
Red = centroid detection  Green = half-max detection
Receiver is on the horizontal axis of the diffraction pattern
X = 35   microradians    Y = 0 microradians

LAGEOS
Rotating about the symmetry axis
Viewed from the equator
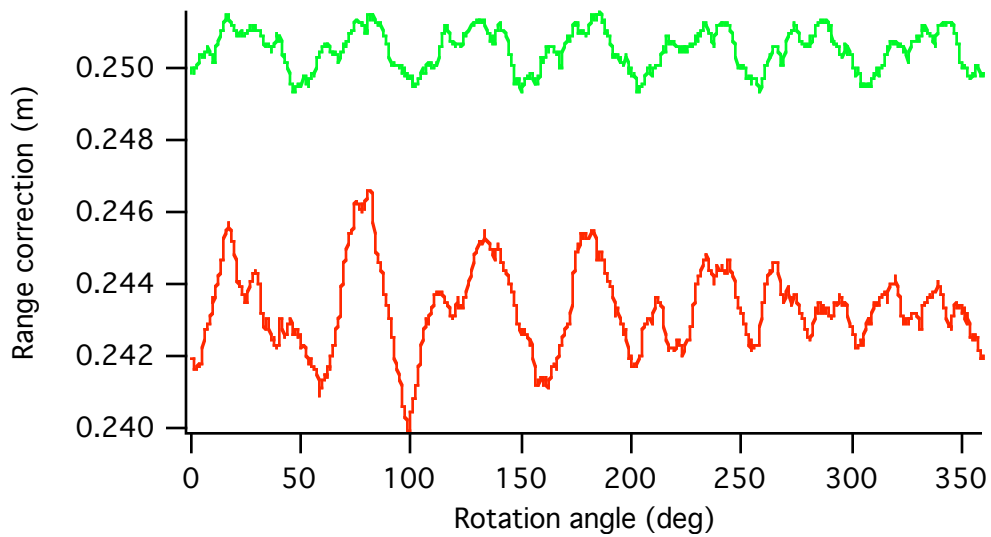


Red = centroid detection  Green = half-max detection

# Comparison of LARES and LAGEOS

The variations in range are reduced by the square root of the number of cube corners. Since there are about 4 times as many cubes on LAGEOS the averaging is better by about a factor of 2.

Because the radius of LARES is about half the size of LAGEOS the range correction is smaller. The variations would be smaller by about a factor of 2 if there were the same number of cubes. Since LARES has fewer cubes the two effects cancel each other approximately so that the variation in the range correction is about the same for both satellites.

## 3. Wavelength correction for LAGEOS 850nm-425nm

This is a preliminary report. No detailed report exists for these analyses. This analysis was done at the request of Stefan Riepl who plans to do two color ranging using circular polarization at wavelengths 850 and 425 nm.
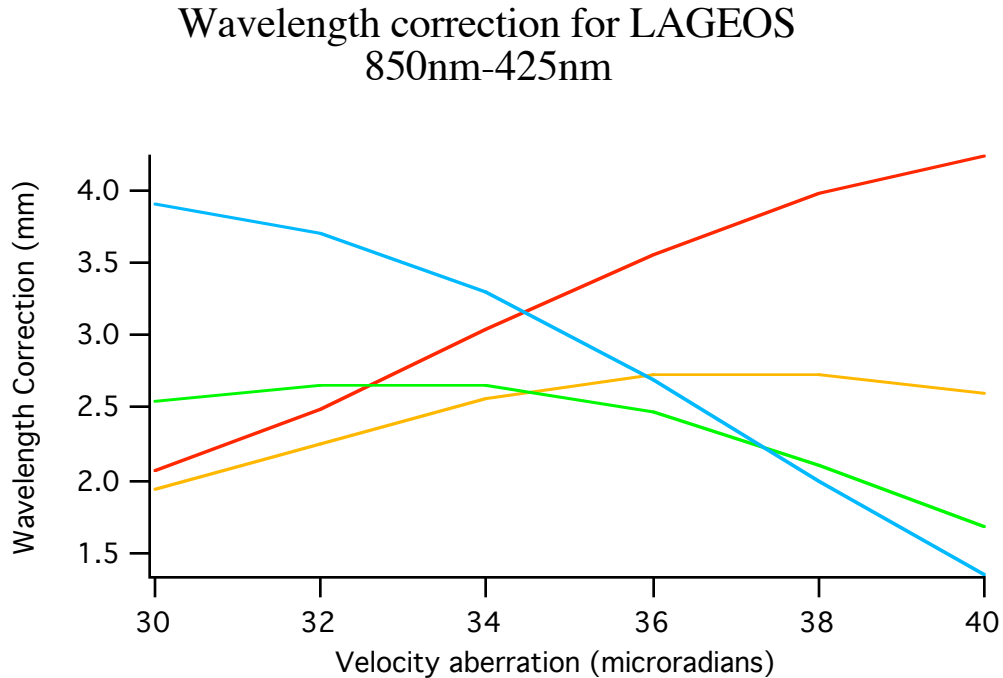


Figure 1. Wavelength correction vs velocity aberration for four dihedral angle offsets.

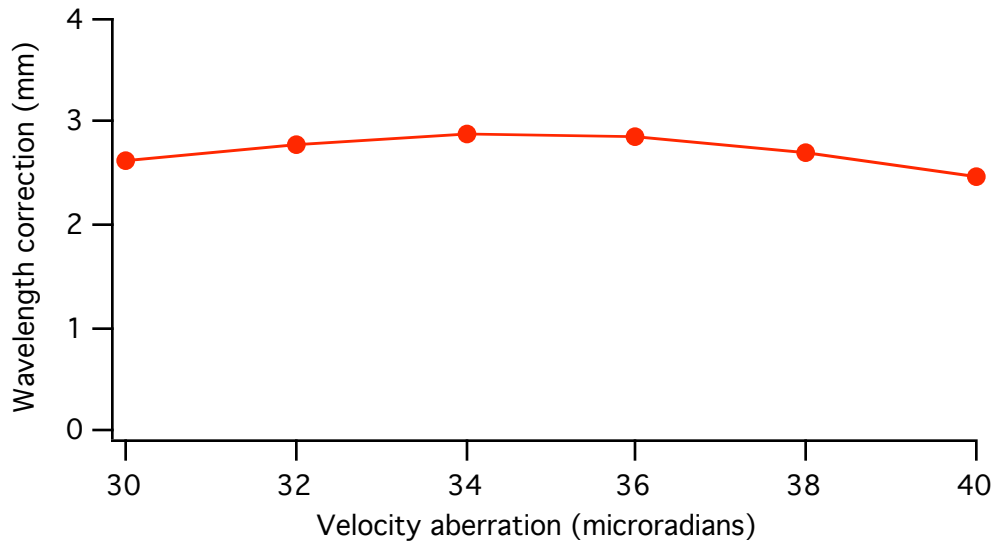| Curve | Dihedral (arcseconds) |
|---|---|
| **Red** | **1.00** |
| **Orange** | **1.25** |
| Green | 1.50 |
| **Blue** | **1.75** |

Figure 2. Wavelength correction vs velocity aberration averaged over four dihedral angle offsets.

| Microradians | 1.00 | 1.25 | 1.50 | 1.75 |
|---|---|---|---|---|
| 30.000000 | 2.064000 | 1.944000 | 2.537000 | 3.915000 |
| 32.000000 | 2.494000 | 2.249000 | 2.648000 | 3.703000 |
| 34.000000 | 3.035000 | 2.560000 | 2.664000 | 3.308000 |
| 36.000000 | 3.568000 | 2.735000 | 2.467000 | 2.691000 |
| 38.000000 | 3.978000 | 2.725000 | 2.098000 | 1.984000 |
| 40.000000 | 4.242000 | 2.592000 | 1.683000 | 1.346000 |

Table 1. Data used to plot Figure 1 in millimeters. The dihedral angle is listed in arcseconds above each column.

| 30 | 32 | 34 | 36 | 38 | 40 |
|---|---|---|---|---|---|
| 2.615000 | 2.773500 | 2.891750 | 2.865250 | 2.696250 | 2.465750 |

Table 2. Data used to plot the average wavelength correction (mm) in Figure 2. The velocity aberration in microradians is listed above each entry.

The range bias is the result of three physical effects.

## A. Diffraction

The diffraction pattern is different at each wavelength. As a result the contribution of each retroreflector is different at each wavelength. This results in a variation of a few millimeters in the range bias at different parts of the diffraction pattern. If the dihedral angle offset is optimized for the velocity aberration the average effect of diffraction is minimized. In the tables, the range bias is smallest at around 1.5 arcsec and increases for larger or smaller dihedral angle offsets.

## B. Refraction

In a solid cube corner the light is bent into the cube corner by refraction at the front face of the cube. The refraction depends on the phase velocity Vp. The phase index of refraction is $Np = c/Vp$. A larger Np increases the acceptance angle of the cube corner and gives larger signal for cubes at large incidence angles. For a circular array the effect is that the centroid closer to the center of the array for larger Np. This makes the range correction smaller.

## C. Group velocity

The optical path length depends on the group velocity Vg of the light in the quartz. The group index of refraction is $Ng = c/Vg$.

| wavelength | phase index | group index |
|:---:|:---:|:---:|
| 0.355 | 1.476 | 1.533 |
| 0.4235 | 1.468 | 1.508 |
| 0.532 | 1.461 | 1.484 |
| 0.85 | 1.452 | 1.465 |
| 1.064 | 1.450 | 1.462 |

Table 3. Np and Ng vs wavelengths (microns) provided by Stefan Riepl.

| Dihedral | Diffraction | Refraction | Group Vel. | Total |
|----------|-------------|------------|------------|-------|
| 0.75 | 2.46 | 0.98 | 1.23 | 4.67 |
| 1.50 | 0.29 | 0.94 | 1.23 | 2.46 |

Table 4. The contribution to the range bias (mm) from each of the three physical effects.

The values in Table 4 are the average for velocity aberration 32, 34, 36, and 38 microradians. The contributions from Refraction and Group Velocity do not change much as the dihedral angle offset changes. The changes are due almost entirely to diffraction effects.

Simulations for LAGEOS with various dihedral angle offsets give the following range bias (850nm-425nm). The wavelength correction is most stable if the dihedral angle is optimized for the particular velocity aberration.

| Dihedral Angle (arcsec) | Range Bias (mm) |
|-------------------------|-----------------|
| 0.00 | 13.18 |
| 0.25 | 10.91 |
| 0.50 | 7.23 |
| 0.75 | 4.67 |
| 1.00 | 3.24 |
| 1.25 | 2.56 |
| 1.50 | 2.46 |
| 1.75 | 2.92 |
| 2.00 | 4.52 |
| 2.25 | 6.66 |
| 2.50 | 10.18 |

Table 5. Wavelength correction (mm) vs dihedral angle offset (arcseconds)

The data in this report are based on simulations at a large number of orientations of the satellite. Data points were at 2 deg intervals in longitude at the equator with fewer points near the poles. The points were on and between each row of cube corners in latitude. At each orientation simulations were done for both wavelengths and 4 different dihedral angle offsets. About 19000 simulations were averaged to obtain the final results.

**Summary. The average wavelength correction between 32 and 38 microradians is 2.806 mm +/- .2 mm.**

## 4. Cross section of the APOLLO Lunar retroreflector array.

The full report on this analysis is listed on the webpage

http://ilrs.gsfc.nasa.gov/satellite_missions/index.html

The APOLLO Lunar retroreflector arrays use a 1.5 inch diameter uncoated fused silica retroreflector with no intentional dihedral angle offset. The front face is recessed by half the diameter in a cavity with a 1.5 degree flare on the first APOLLO array and a 6 degree flare on the two later arrays. This reduces the cross section for incidence angles beyond 6 degrees. The cutoff angle with no flare would be 27.7 degrees. With the 1.5 degree flare it is 28.3 degrees. With the 6 degrees flare it is 30.3 degrees. The maximum velocity aberration for ranging to the moon from earth is about 10 microradians. This puts the receiver on the central peak of the diffraction pattern. The maximum incidence angle due to the moon's libration pattern is about 10 degrees.
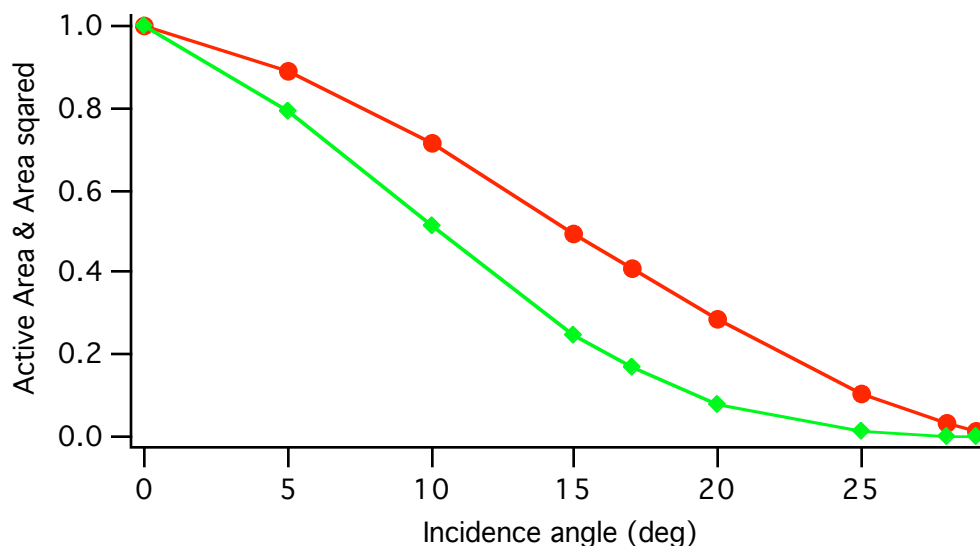


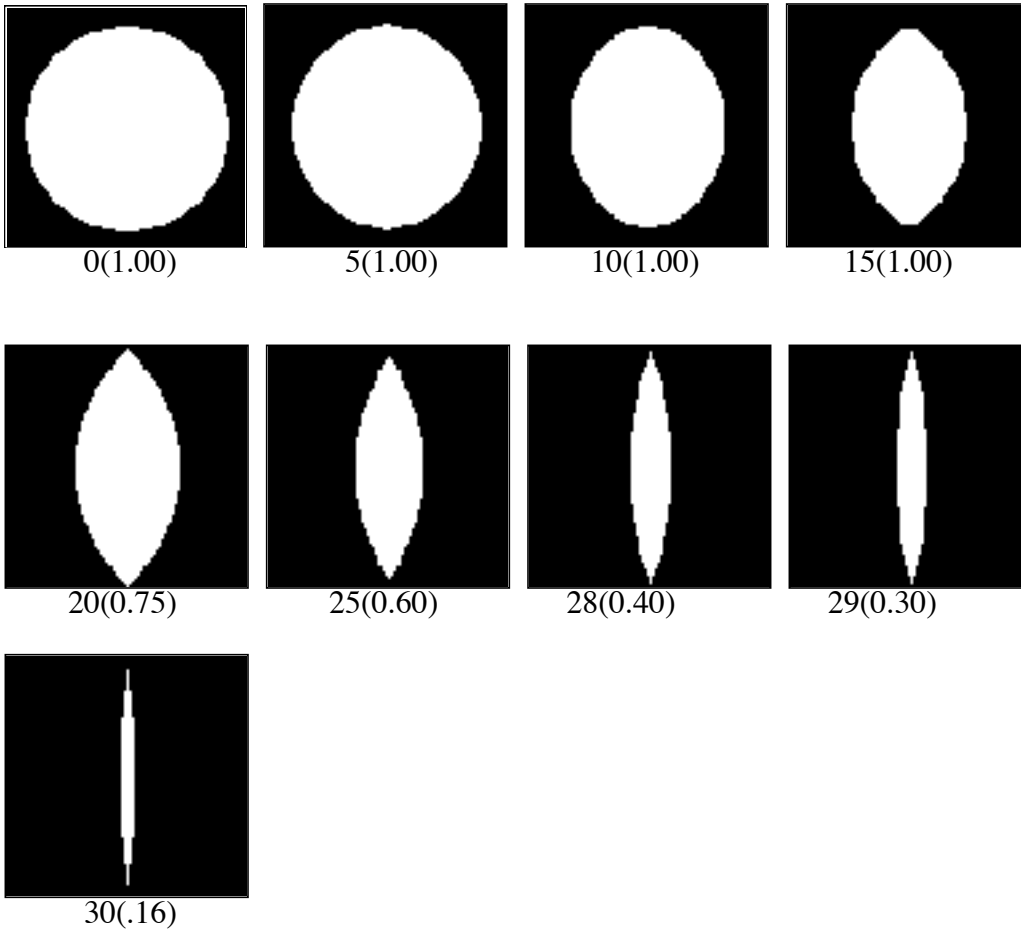Figure 1. Active reflecting area and square of the active reflecting area vs incidence angle $\phi$.

Figure 3. Shape of the active reflecting area vs incidence angle $\phi$. The incidence angle is listed below each figure. The number in parenthesis is the pixel size which has been reduced for the larger incidence angles in order to give better resolution as the active reflecting area decreases.

Since the APOLLO retroreflectors are uncoated, there is loss of total internal reflection at certain incidence angles. Figure 4 below shows incidence angles where there is loss of total internal reflection.
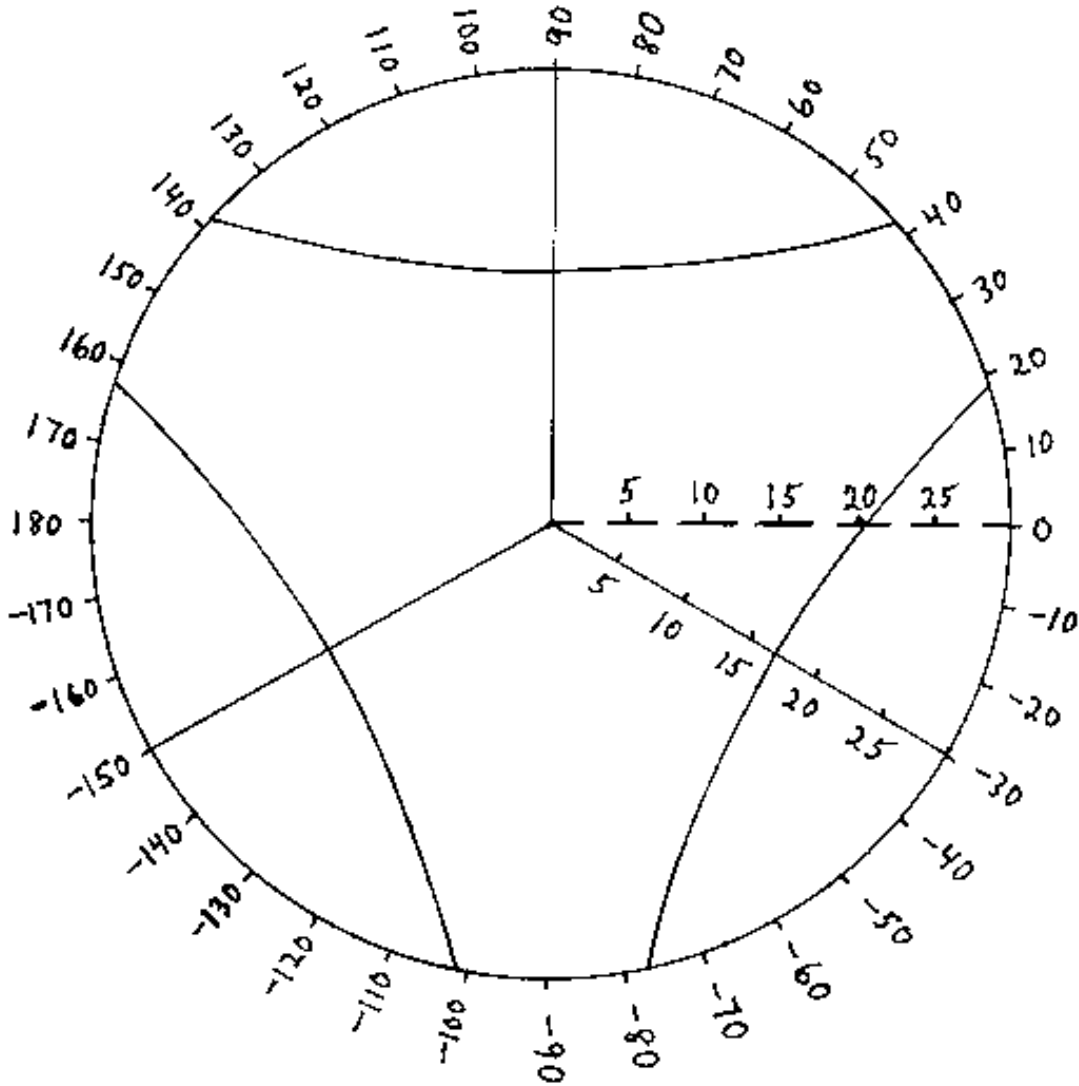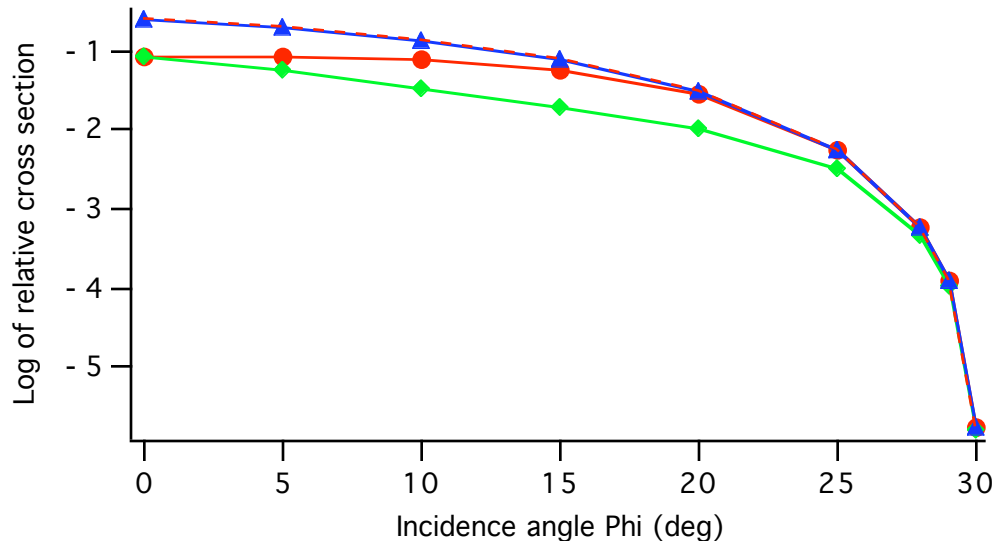


Figure 4. Total internal reflection diagram for an APOLLO retroreflector.

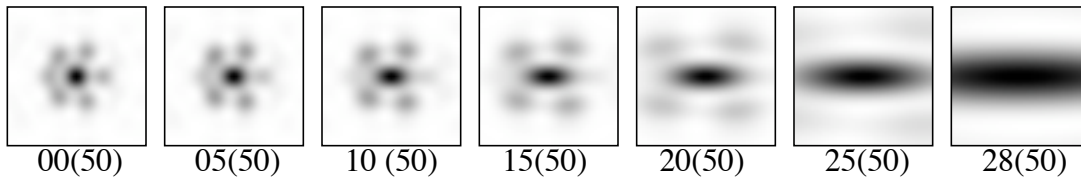# Cross section at θ = +30 deg

## Vertical polarization
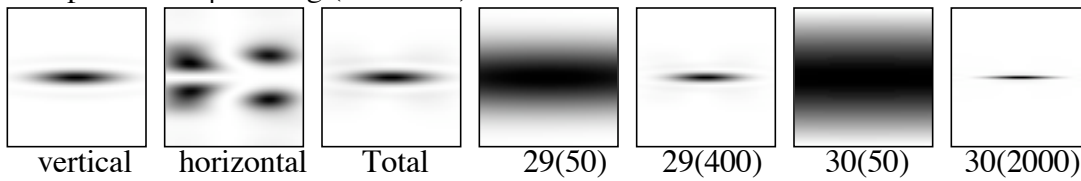


Red        (10,0)
Green      (0,10)
Blue       (0,0)
Magenta    Maximum

The cross section is plotted at four different points in the far field diffraction pattern. The coordinates (x,y) in microradians are listed for each color curve. The red curve is on the horizontal axis at (10,0) microradians. The Green is along the vertical axis at (0,10). The blue is at the center at (0,0). The magenta is the maximum and coincides with the blue curve. The polarization is perpendicular to the plane of incidence (vertical). At this orientation there is no loss of total internal reflection.

# Diffraction patterns at each incidence angle
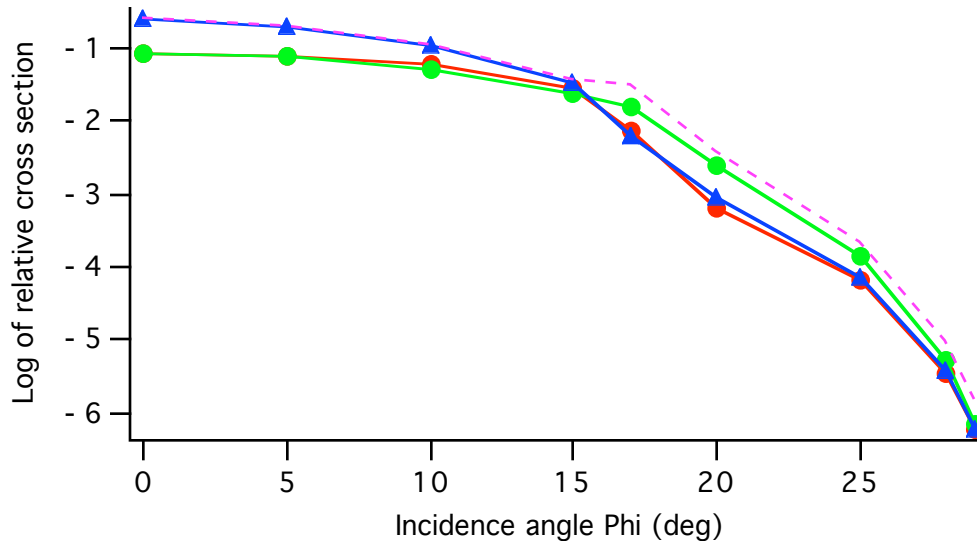## θ = +30 deg, Vertical polarization



| 00(50) | 05(50) | 10 (50) | 15(50) | 20(50) | 25(50) | 28(50) |

Components at φ=28 deg (scale 200)



| vertical | horizontal | Total | 29(50) | 29(400) | 30(50) | 30(2000) |

The incidence angle is shown below each plot in deg with the scale in microradians in parenthesis. The components of the pattern are shown at one incidence angle (28 deg).

## Cross section at θ = -30 deg
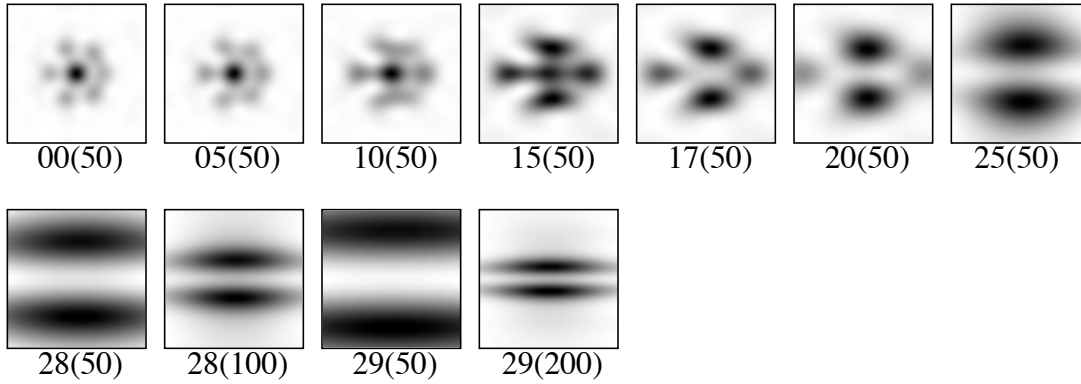
### Vertical polarization



Red        (10,0)
Green      (0,10)
Blue       (0,0)
Magenta    Maximum

The cross section is plotted at four different points in the far field diffraction pattern. The red curve is a point along the horizontal axis at (10,0) microradians. The Green is along the vertical axis at (0,10) microradians. The blue is at the center (0,0) microradians. The magenta curve is the maximum intensity. The polarization is perpendicular to the plane of incidence (vertical). At this orientation there is loss of total internal reflection at about $\phi = 17$ degrees. There is a discontinuity in the slope of the curve at this point.

Diffraction patterns at each incidence angle
$\theta$ = -30 deg, Vertical polarization

| 00(50) | 05(50) | 10(50) | 15(50) | 17(50) | 20(50) | 25(50) |

| 28(50) | 28(100) | 29(50) | 29(200) |

The incidence angle in degrees is shown below each pattern with the scale in microradians in parenthesis.

# Diffraction patterns at each incidence angle
## $\theta = 0$ deg, Vertical polarization
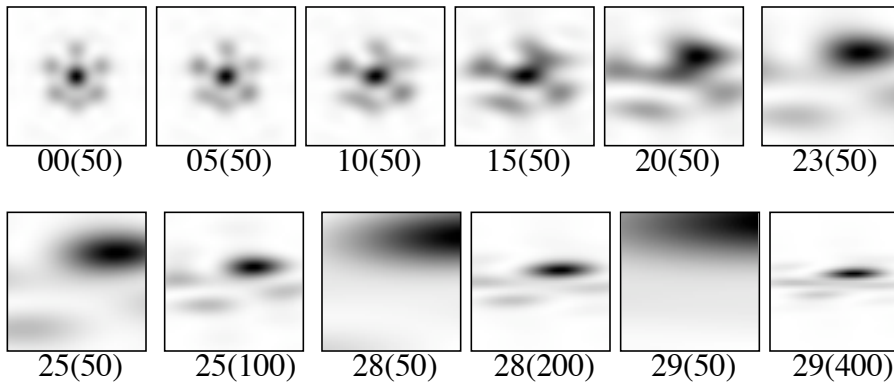


| 00(50) | 05(50) | 10(50) | 15(50) | 20(50) | 23(50) |

| 25(50) | 25(100) | 28(50) | 28(200) | 29(50) | 29(400) |

The incidence angle in degrees is shown below each pattern with the scale in microradians in parenthesis.

## 5. Parametric thermal analysis of hollow cubes.

This section gives excerpts from a detailed (but unpublished) report that is available on request.

Equations have been derived for making order of magnitude estimates of the thermal gradients in a hollow Beryllium retroreflector due to absorption of solar radiation. The equations show the dependence on factors such as the area, thickness, solar absorptivity, conductivity, and emissivity of the reflecting plates. The performance of the retroreflector can be degraded by thermal warping of the plates or changes in the dihedral angles between the reflecting plates as a result of differential expansion and contraction.

**Conduction through the plate.**

If we have a plate in free space that is subjected to solar radiation on one side, the side facing the sun will be warmer than the side facing empty space. The thermal expansion of the side facing the sun will be greater than the thermal expansion on the back side. This will result in the side facing the sun being slightly convex and the side facing empty space being slightly concave. The objective of this analysis is to calculate the amount of buckling of the plate in order to see if it will cause a significant distortion of the wavefront reflected from the surface.

Suppose we have a square plate of area $l$ x $l$ and thickness $w$. The thermal parameters are

$\alpha$ = solar absorptivity
$\varepsilon_1$ = emissivity of the front surface
$\varepsilon_2$ = emissivity of the back surface
$S$ = solar constant = 1412.5 Watts/sq meter
$k$ = thermal conductivity of Beryllium = 225 Watts/m-°K
$c$ = linear expansion coefficient of Beryllium = $11.3 x 10^{-6} K^{-1}$
$\sigma$ = Stefan Boltzman constant = $5.6697 x 10^{-8} W m^{-2} K^{-4}$

The deflection of one side of the plate due to conduction through the plate in terms of the parameters above is given by

$$d = \frac{lclf\alpha Sw}{2wk} = \frac{cl^2 f\alpha S}{2k}$$

## Conduction along a plate.

The linear expansion of the plate due to conduction along the plate is given by the equation

$$d = \frac{cf\alpha S l^3}{kw}$$

Putting numbers into the equations shows that conduction through the plate is not a problem because the conduction path is wide and the path length short. However, conduction along the plate can be a problem because the path length is long and the conduction path is narrow. Thermal distortion of the plates is acceptable as long as the cube corner is not larger than about 2 inches and the plate has a low solar absorptivitiy such as 7 percent.

## 6. Retroreflector arrays for high altitude satellites.

The data in the tables below shows options for obtaining a cross section of 100 million sq meters at the altitude of the GNSS satellites and a cross section of one billion sq meters at geosynchronous altitude. A detailed report was presented at the EGU conference in Vienna in April, 2006.

# Retroreflector area and mass

### Galileo

| Design | # of cubes | Diam. in | Area sq cm | Mass g |
|--------|-----------|----------|-----------|--------|
| uncoated | 50 | 1.3 | 428 | 1000 |
| coated | 400 | 0.5 | 508 | 460 |
| hollow | 400 | 0.5 | 508 | 201 |
| hollow | 36 | 1.4 | 356 | 400 |
| GPS | 160 | 1.06 | 1008 | 1760 |

### Geosynchronous

| Design | # of cubes | Diam. In. | Area sq cm | Mass g |
|--------|-----------|-----------|-----------|--------|
| Uncoated | 165 | 1.7 | 2415 | 7457 |
| Coated | 1153 | .7 | 2863 | 3638 |
| Hollow | 1153 | .7 | 2863 | 1590 |
| Hollow | 122 | 1.8 | 2003 | 2863 |
| Single dihedral | 22 | 2.0 | 446 | 708 |

## Array area and mass

### GPS

| Design | # of cubes | Diam. in | Area sq cm | Mass g |
|---|---|---|---|---|
| uncoated | 50 | 1.3 | 847 | 2310 |
| coated | 400 | 0.5 | 1005 | 1062 |
| hollow | 36 | 1.4 | 587 | 1144 |

### Geosynchronous

| Design | # of cubes | Diam. In. | Area sq cm | Mass g |
|---|---|---|---|---|
| Uncoated | 165 | 1.7 | 4782 | 17,218 |
| Coated | 1153 | .7 | 5668 | 8400 |
| hollow | 122 | 1.8 | 3305 | 8217 |

The estimates of array mass were made by scaling from similar arrays on existing satellites.

## 7. Measurements of Russian cube corners

A detailed report is available on these measurements. Excerpts from the report are given below. The data used in this analysis were kindly provided by Vladimir Vasiliev. A measurement of a reference mirror the same size as the cube corner is used for absolute calibration of the cross section of the cube corner.

## Normalized patterns

Figure 7 shows the normalized patterns for the reference mirror and cube corner. The cube corner is a very high quality diffraction limited cube.



A. Mirror                    B. Retroreflector
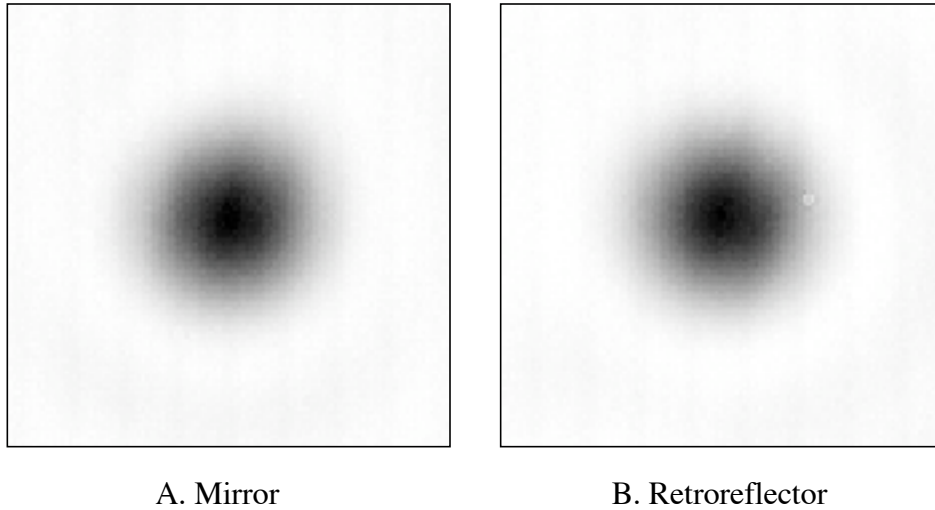
Figure 7. Diffraction patterns of reference mirror and cube corner normalized to 100%.
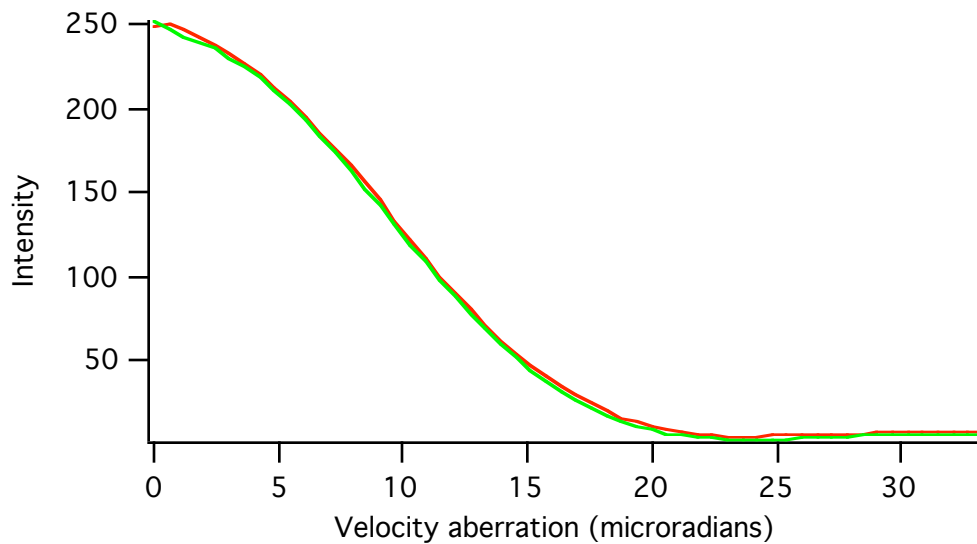


Figure 13. Plot of cross section vs velocity aberration for the mirror and cube corner. The patterns have essentially the same shape. The values are the average around a circle in the pattern.
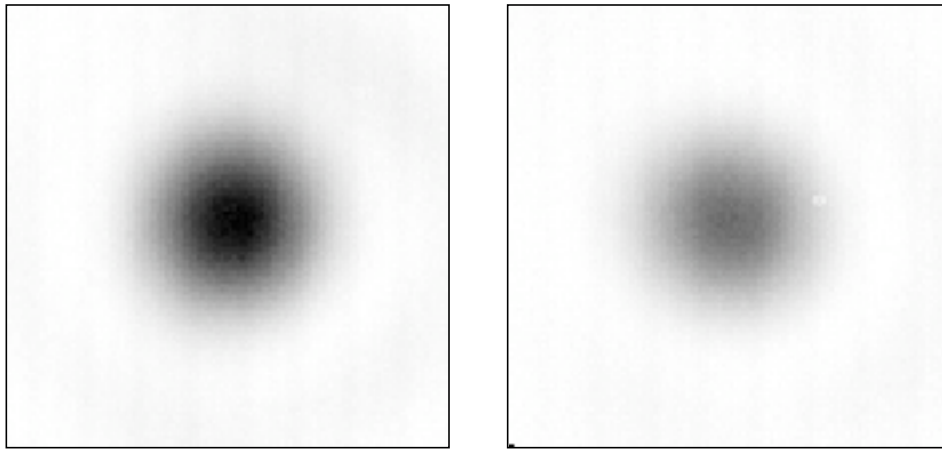
A. Mirror

B. Retroreflector

Figure 14. Diffraction patterns of reference mirror and cube corner measured at the same scale.
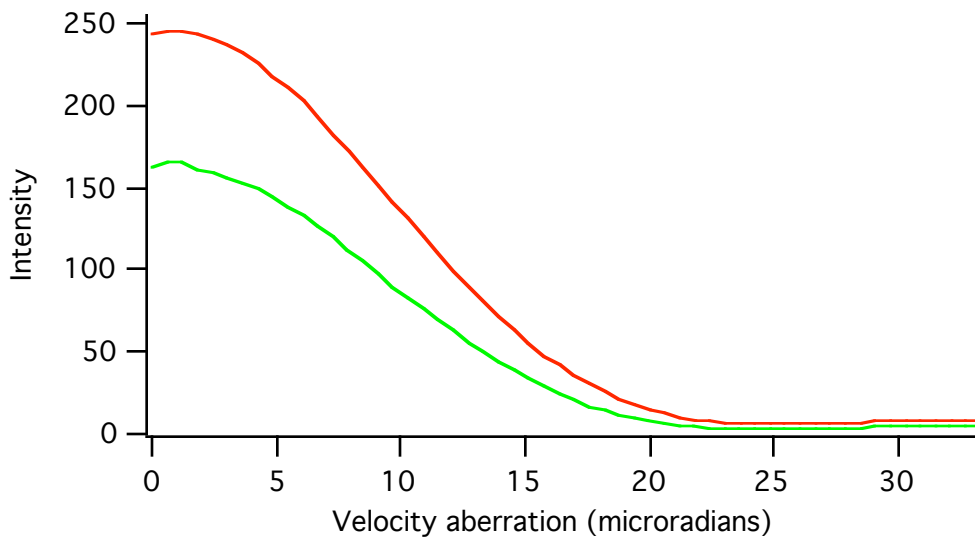


Figure 15. Normalized and fixed scale measurements of the cube corner for case A.
Red = normalized
Green = fixed scale
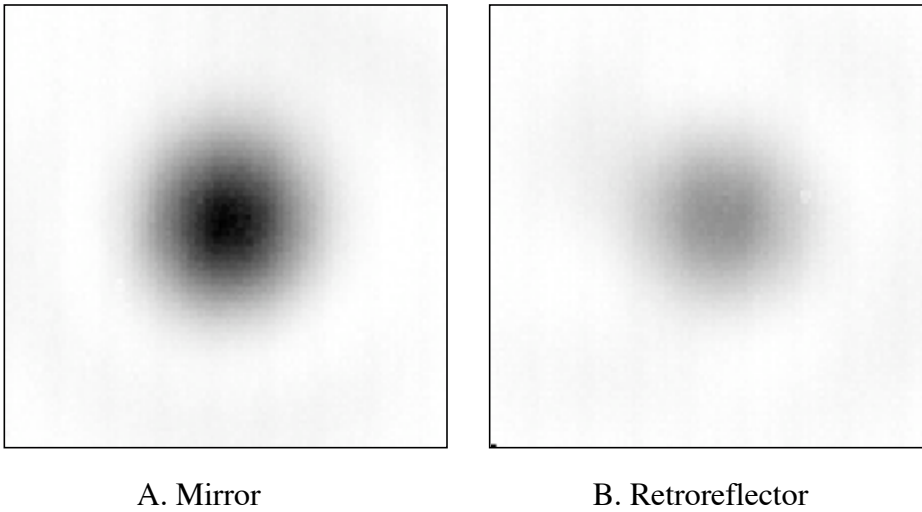
A. Mirror                    B. Retroreflector

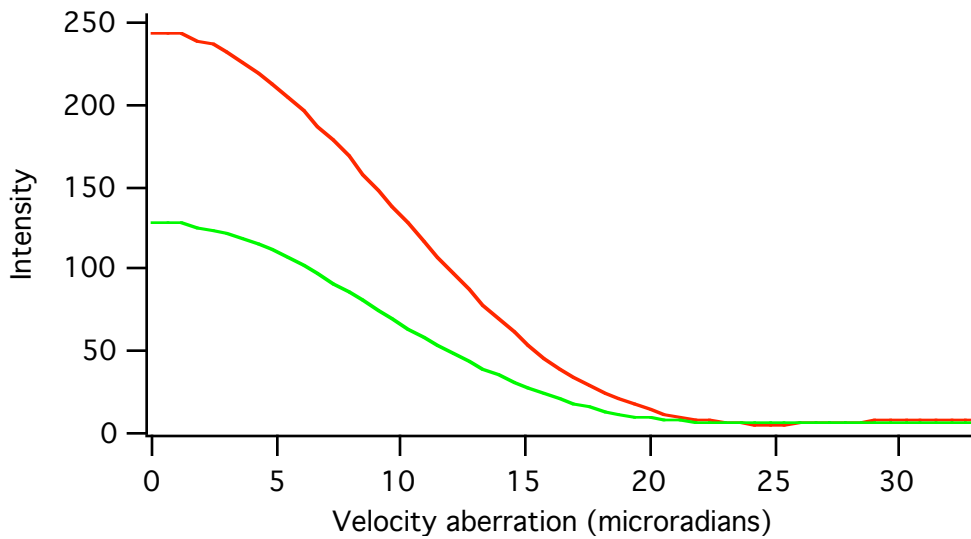Figure 18. Diffraction patterns of reference mirror and a typical Glonass cube corner measured at the same scale.



Figure 19. Cross section of the reference mirror and a typical cube corner vs velocity aberration.
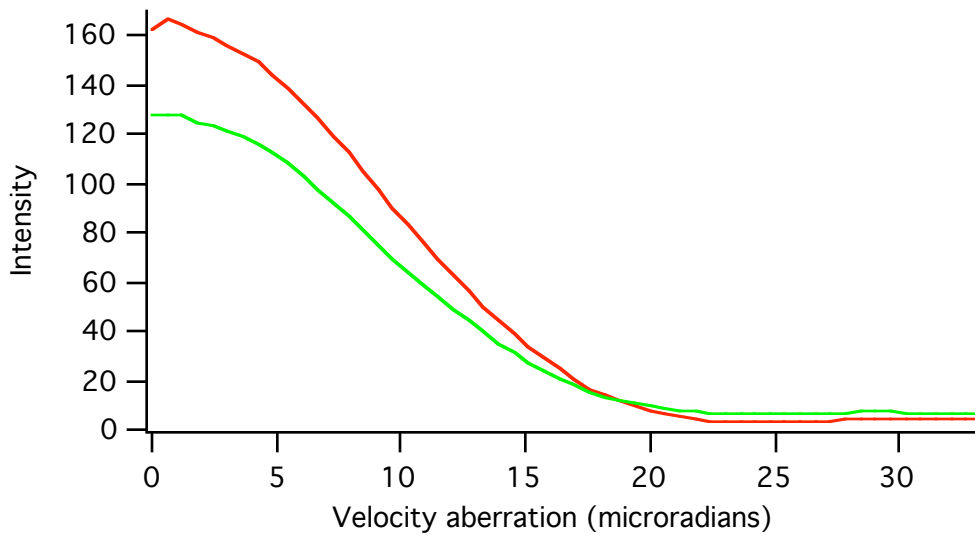
Figure 20. Cross section of good cube corner at fixed scale and typical Glonass cube corner vs velocity aberration.
Red = good cube measured at fixed scale
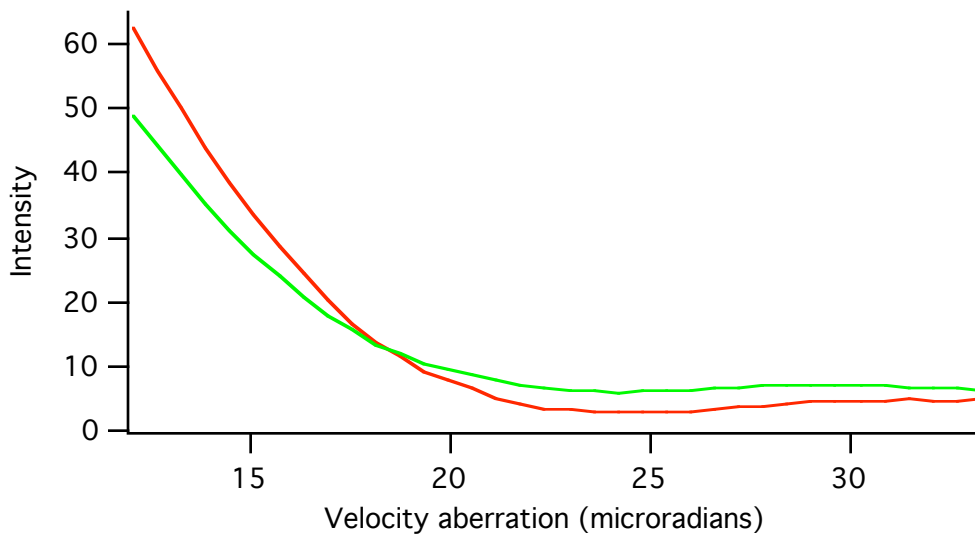Green = typical Glonass cube corner measured at fixed scale



Figure 21. Cross section of good cube corner and typical Glonass cube corner vs velocity aberration showing the cross section at larger values of velocity aberration. The cross section of the typical cube is larger than that of a diffraction limited cube corner past about 20 microradians.

## 8. Thermal simulations of Russian cube corner.

These simulations were done using a very simple thermal simulation program. It is not a high fidelity model and has been used only to give order of magnitude effects.

The detailed thermal parameters of the Russian cube corners and mounting structure are not available so a realistic simulation cannot be done. These are parametric studies using assumed values of the thermal parameters.
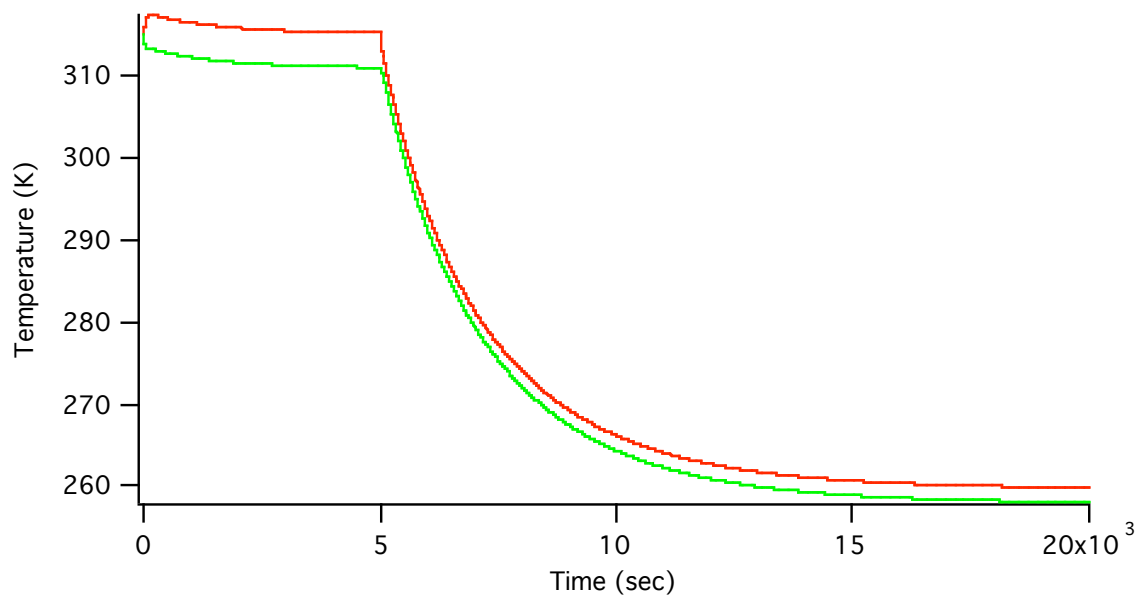


Red = vertex
Green = center of front face.

Temperature of the vertex and front face vs time. The cube is initialized to 315 deg K with a solar simulator on at normal incidence to the front face. The mounting cavity is at 300 deg K. The effective emissivity of the cavity is 50%. The emissivity of the front face is .85. The reflectivity of the aluminum back faces is .85 per surface (.614 for three reflections). Absorption of solar radiation by the quartz and conductivity of the mount are not modeled. The solar simulator is turned off at 5000 sec.
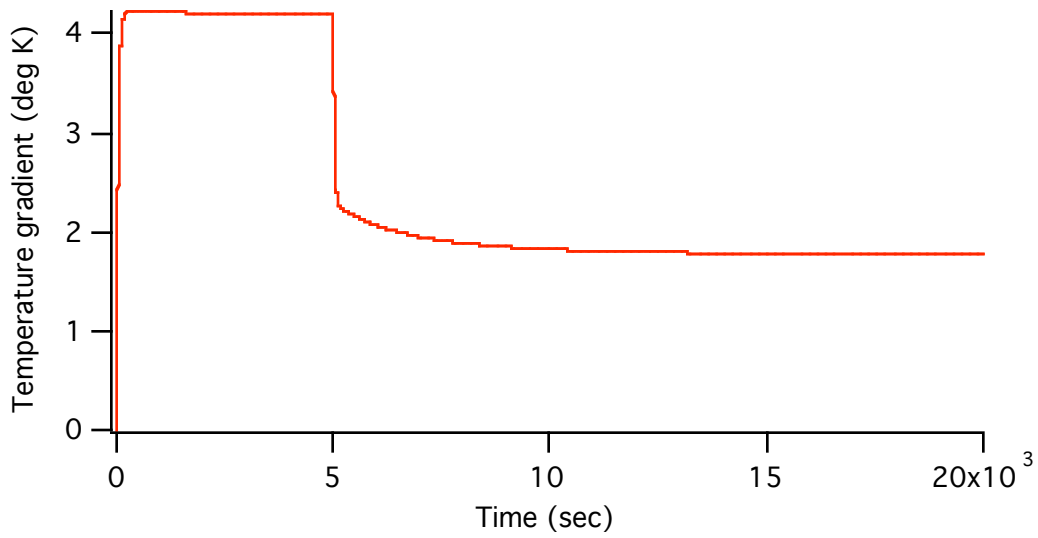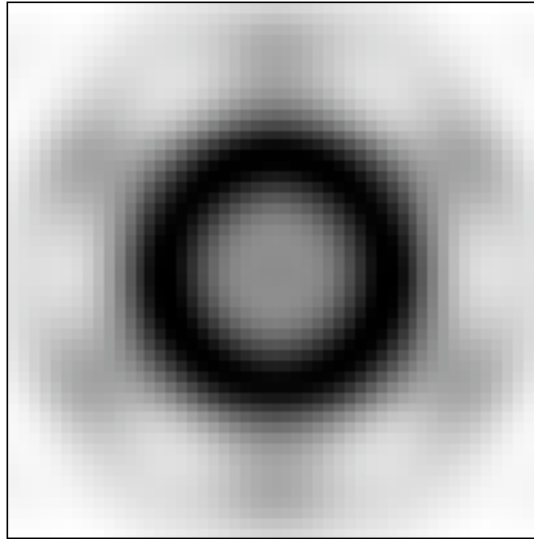
Temperature difference between the vertex and the center of the front
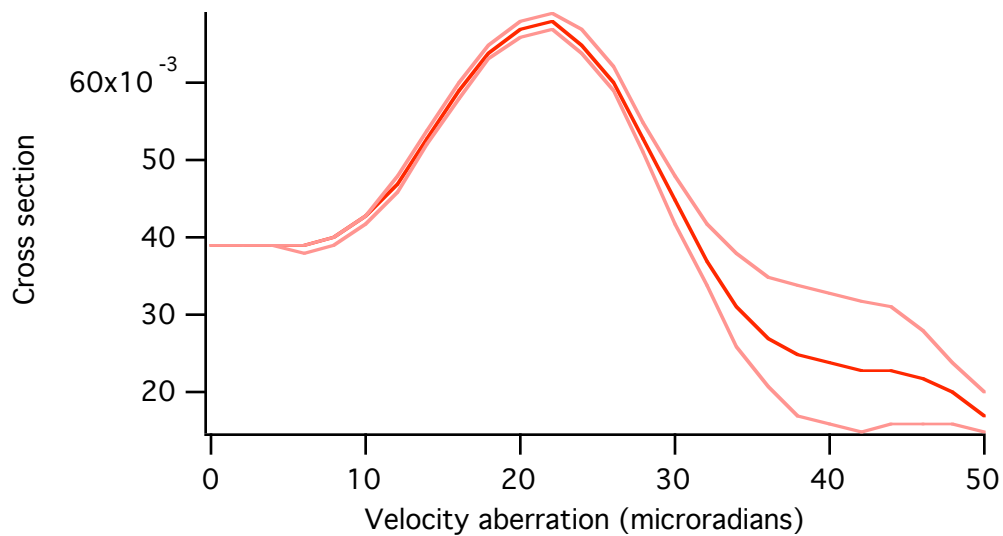face vs time.
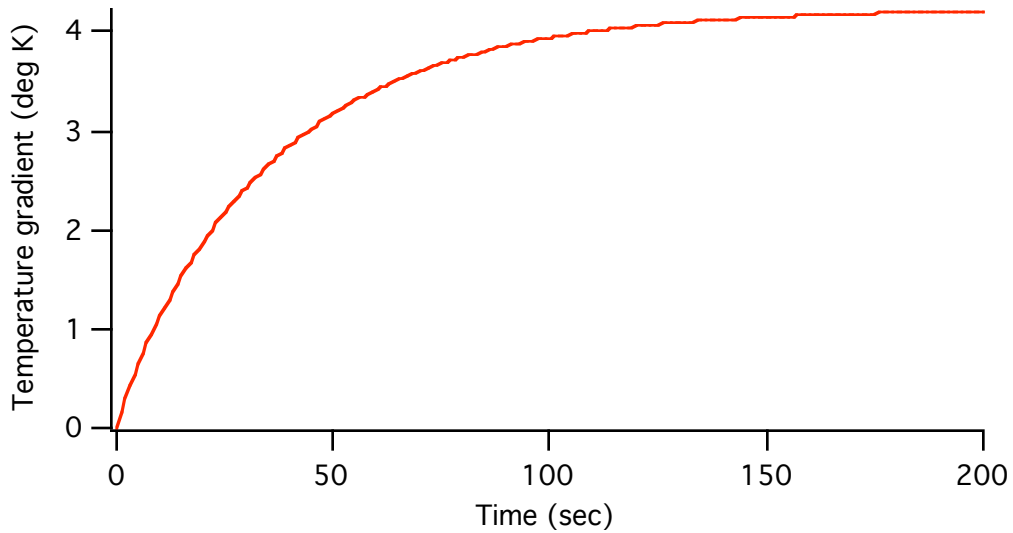


Temperature difference between the vertex and the center of the front
face from 0 to 200 seconds.
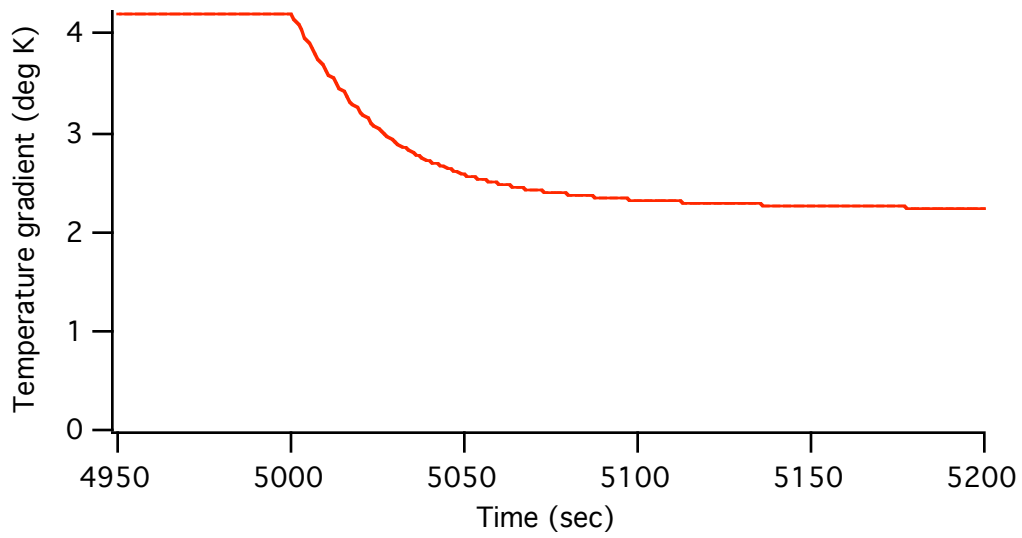
Temperature difference between the vertex and the center of the front face from 4950 to 5200 seconds.
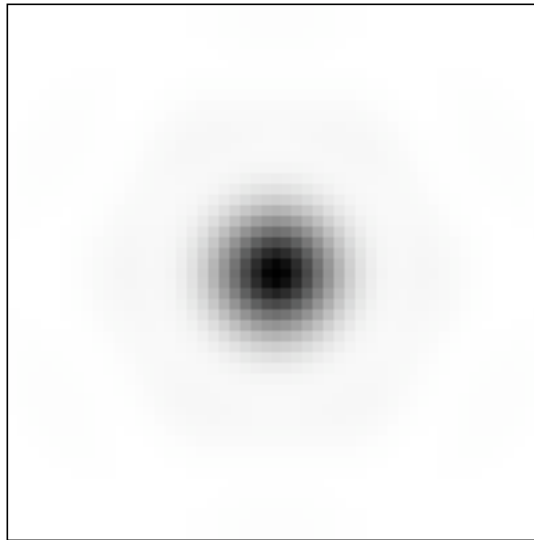
Diffraction pattern before the solar simulator is turned off at 5000 seconds. Scale is -50 to +50 microradians in each dimension.



Red = average
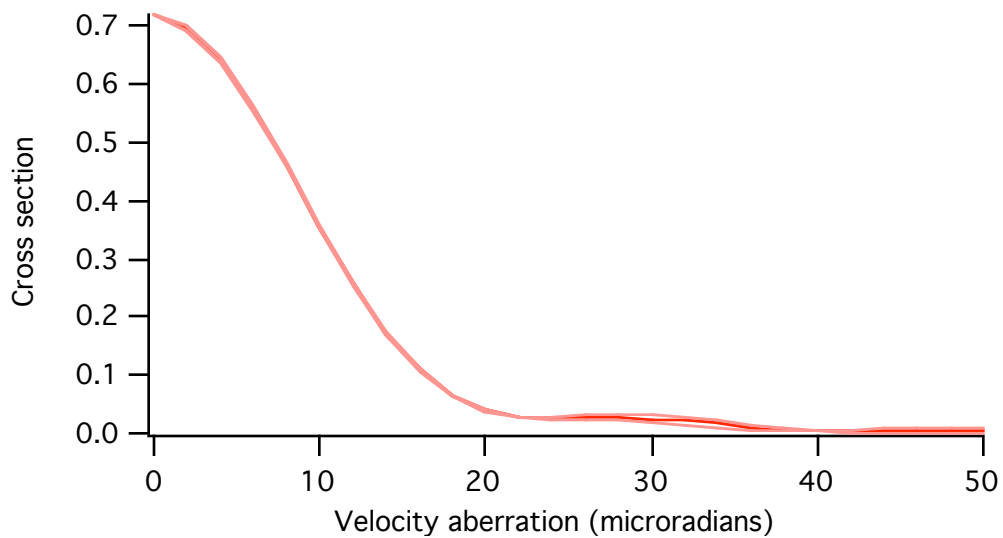Pink = minimum and maximum values around a circle in the far field.

Cross section vs velocity aberration at 5000 seconds before the solar simulator is turned off. The cross section is in units of 10.5 million sq meters. The cross section at 26 microradians is .06 which is .63million sq meters per cube. For 32 cubes this is 20 million sq meters which is the nominal cross section for GPS.

Diffraction pattern at the end of the simulation at 20,000 seconds.

Cross section vs velocity aberration at 20,000 seconds. The cross
section at 26 microradians is ..027 in these units which is .28 million
sq meters per cube. For 32 cubes this is 9 million sq meters. This is
about half the nominal cross section of 20 million sq meters for GPS.
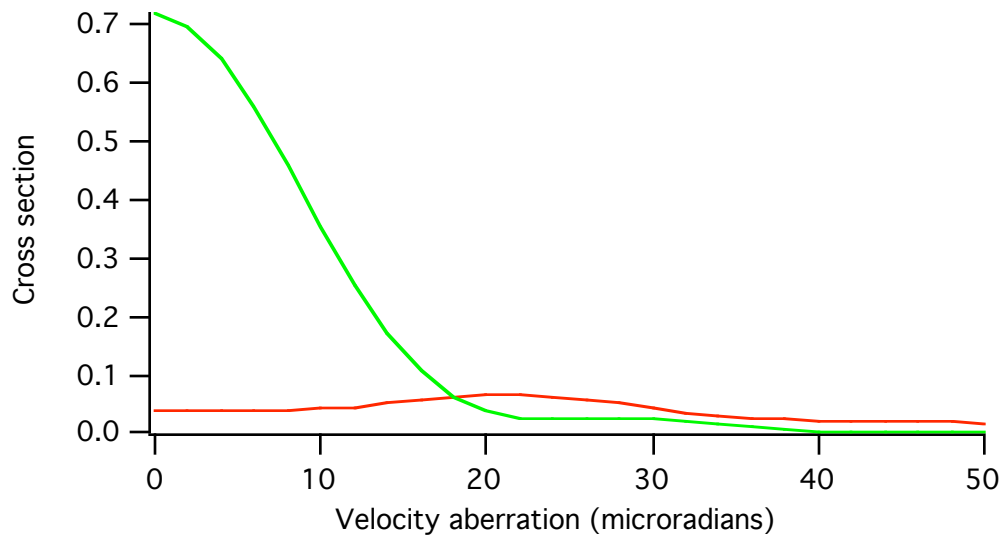
Comparison of cross section vs velocity aberration with solar illumination (red) and without solar illumination (green). The patterns are completely different. The central peak drops from .7 to .04 with solar illumination. The cross section at 26 microradians is about twice as great with solar illumination. The units are such that the amplitude of the central peak is unity for a perfect reflector. With Fresnel reflection losses at the front face the maximum amplitude is .93 in these units.

These results suggest that thermal effects could, in principle, cause significant variations in the diffraction pattern. However, the actual behavior could be quite different from the simulations since the thermal parameters of the cube corner and mounting structure are not available. In the absence of a reliable simulation the only way to know how the Russian cube corners behave is by laboratory testing.

## 9. Laboratory tests of cube corners.

The space climactic facility at LNF in Frascati, Italy presently has a section of the LAGEOS retroreflector array, a section of LARES cube corners, and the third GPS array which contains Russian cube corners. The plan is to take diffraction patterns similar to those described in section 7 of this report and do thermal vacuum test to measure the response of the cube corners to solar radiation. These test results can be compared to the simulations given in section 8 of this report. There will probably be significant differences between the simulations and the laboratory tests because of the limitations in the modeling.

## 10. Modeling of the response of a SPAD detector to a distributed signal.

This section is a question, not a statement.

The analysis programs that I use can compute the range correction of a retroreflector array for centroid and constant fraction detectors. They cannot compute a range correction for a SPAD detector because I have no clear understanding of how the current rises after a photon is detected. The usual assumption is that the range correction is the distance to the first retroreflector since the SPAD triggers on the first photoelectron.

One possible model of a SPAD is that the number of charge carriers increases exponentially after a photon is detected until saturation effects set in as a result of the finite number of available charge carriers. Until saturation sets in the number of carriers $n$ vs time $t$ is given by

$$n = e^t$$

Tom Murphy has suggested that the dependence of the number of charger carriers is closer to

$$n = t^2$$

The reasoning is that the charger carriers are contained in a thin layer. The area of conduction is a disc whose radius increases linearly with time by thermal diffusion of the charger carriers. The area of the disc is proportional to the square of the radius.

The rise time of a real SPAD detector is a function of the number of photoelectrons. This effect is used to calibrate the response vs signal strength by ranging to a flat target. In the exponential model the rise time is independent of the number of photoelectrons. The quadratic model does give a dependence of the rise time on signal strength. However, there are geometrical effects that alter the simple equation in a real SPAD. I have no model for these geometrical effects. Below is an analysis based on an exponential buildup.
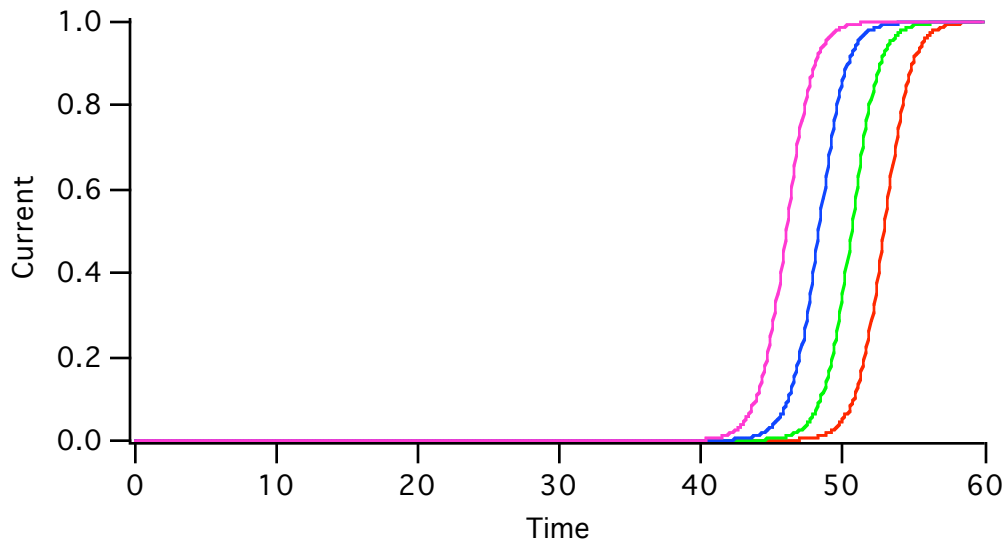
Figure 1. Current vs time for different numbers of starting photoelectrons. The total number of electrons is $N = 10^{23}$.

red         = 1 electron
green       = 10 electrons
blue        = 100 electrons
magenta     = 1000 electrons

In the target tests the change in the time of the 50% Point from 1 to 1000 photoelectrons is about 240 ps. This corresponds to 6.9 time units in the simulation because $\log(1000) = 6.9077$. Using the target tests as a calibration factor to the time units gives $240/6.9 = 34.8$ ps per time unit. In one way range 34.8 ps corresponds to 5.2 millimeters.
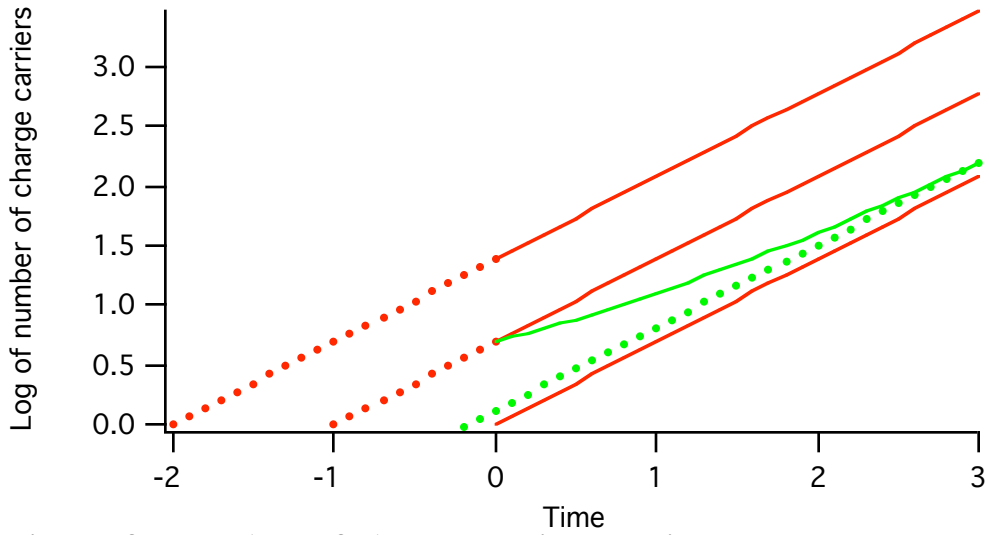
# SPAD with distributed input
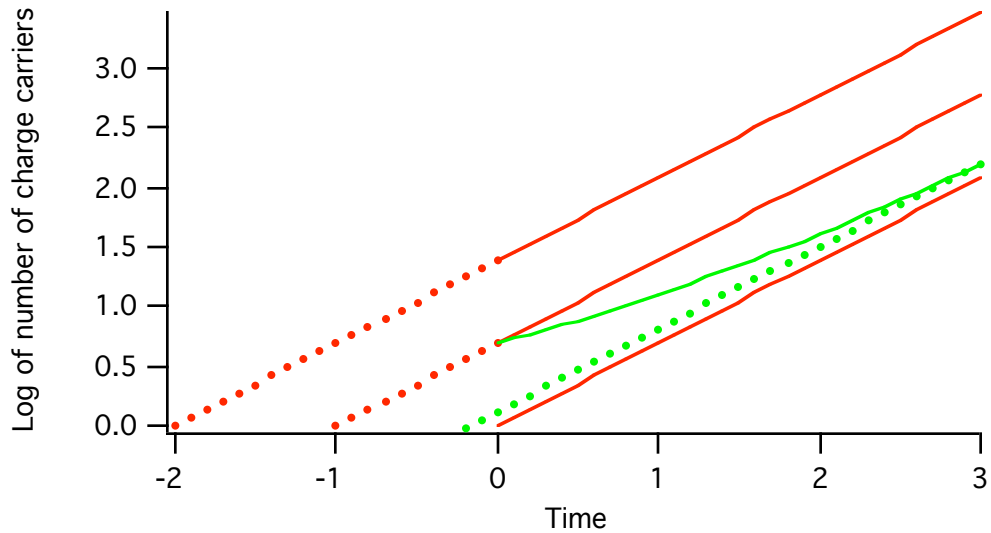


Figure 2. Number of charge carriers vs time.

The values along the lines in linear units are

| Case | Color | Line | Time 0 | 1 | 2 | 3 |
|------|-------|--------|----|----|----|----|
| 1 | Green | Curve | 02 | 03 | 05 | 09 |
| 2 | Red | Bottom | 01 | 02 | 04 | 08 |
| 3 | Red | Middle | 02 | 04 | 08 | 16 |
| 4 | Red | Top | 04 | 08 | 16 | 32 |

The values along the vertical axis in linear and logarithmic units are

| n | 2 | 4 | 8 | 16 | 32 |
|--------|-------|-------|-------|--------|--------|
| log(n) | .6931 | 1.386 | 2.079 | 2.7725 | 3.2657 |

The time units in Figure 2 are such that the number of charge carriers increases by a factor of 2 in one time unit. The three straight red lines (cases 2, 3, and 4) are the number of charge carriers vs time with 1, 2, and 4 initial photoelectrons respectively. The dotted lines are extrapolations backward in time. The vertical axis is the natural logarithm of the number of charge carriers.

The green curve (case 1) is one photoelectron more than the bottom red line (case 2). The percentage change in the number of charge carriers in the green curve is less as time increases. The dotted green line is the backward extrapolation of the green curve at $t = 3$ where the number of charge carriers is 9.

In the green curve (case 1) the number of photoelectrons is 2, the same as the middle red curve (case 3). However, the extrapolation back in time gives a different result for cases 1 and 3. Would the rise time of a real SPAD for the case of the green line (case 1) be the same as that of the middle red line (case 3) , or would it be closer to the rise time of the bottom red line (case 1)? What time correction would be applied by the CSPAD to the case of the green line?

Figure 3 plots the effect on the measured time of receiving a second photoelectron vs the time when it is received.
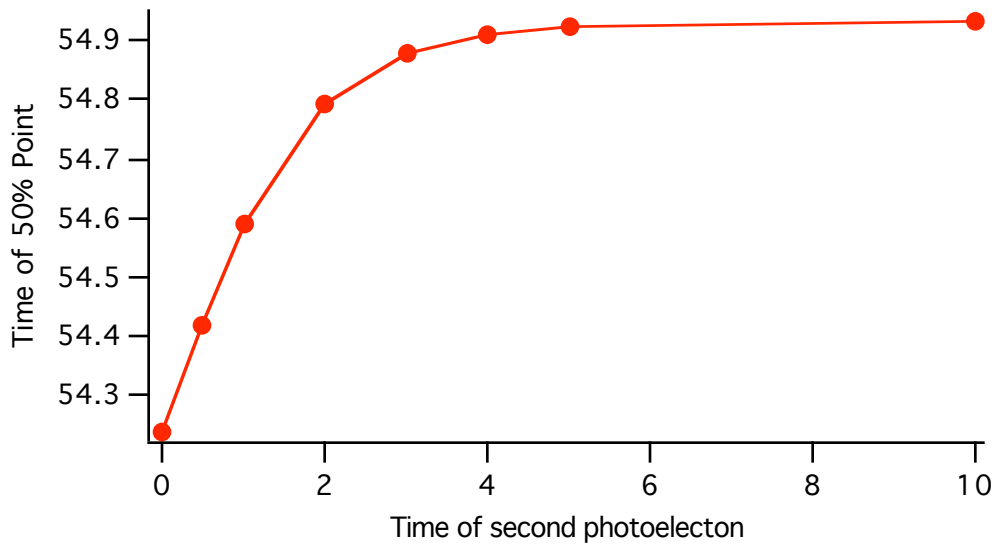


Figure 3. Variation in the time of the 50% point vs the time due to a second photoelectron. There is one photoelecton at time $= 0$.

| Time of 2nd pe | | Time of 50% | Δ50% Point | |
|---|---|---|---|---|
| t | mm | Point | t | mm |
| 0.0 | 0.0 | 52.1995 | 0.6931 | 3.60 |
| 0.5 | 2.6 | 52.3796 | 0.5130 | 2.66 |
| 1.0 | 5.2 | 52.5514 | 0.3412 | 1.77 |
| 2.0 | 10.4 | 52.7532 | 0.1394 | 0.72 |
| 3.0 | 15.6 | 52.8390 | 0.0536 | 0.28 |
| 4.0 | 20.8 | 52.8726 | 0.0200 | 0.10 |
| 5.0 | 26.0 | 52.8852 | 0.0074 | 0.04 |
| 10.0 | 52.0 | 52.8926 | 0.0000 | 0.00 |

Table 1. Time of 50% Point vs time of the second photoelectron.

Conclusions

This analysis may be wrong as a result of using the wrong expression for the number of charge carriers vs time. However, a different expression would probably still come to the same conclusion regarding the change in the time of the 50% point as a result of a second photoelectron received shortly after the first.

In the absence of a good model describing the behavior of a SPAD the only way to know the effect of a photoelectron that arrives a short time after the first is to do an experiment. For example, the target calibration vs signal strength could be done first with a flat target and then with a target where half the area is at position zero and half is a few millimeters farther away.